Research article

Vertical graphene nanowalls supported hybrid W_2C/WO_x composite material as an efficient non-noble metal electrocatalyst for hydrogen evolution

Shahadev Rodriguez-Miguel [a], Yang Ma [a,b], Ghulam Farid [a,b], Roger Amade [a,b], Rogelio Ospina [a,b,c], Jose Luis Andujar [a,b], Enric Bertran-Serra [a,b], Stefanos Chaitoglou [a,b,*]

[a] Department of Applied Physics, University of Barcelona, C/Martí i Franquès, 1, 08028, Barcelona, Catalunya, Spain
[b] ENPHOCAMAT Group, Institute of Nanoscience and Nanotechnology (IN2UB), University of Barcelona, C/Martí i Franquès, 1, 08028, Barcelona, Catalunya, Spain
[c] Escuela de Física, Universidad Industrial de Santander, Carrera 27 calle 9 Ciudad Universitaria Bucaramanga, Colombia

A B S T R A C T

Research for the development of noble metal-free electrodes for hydrogen evolution has blossomed in recent years. Transition metal carbides compounds, such as W_2C, have been considered as a promising alternative to replace Pt-family metals as electrocatalysts towards hydrogen evolution reaction (HER). Moreover, hybridization of TMCs with graphene nanostructures has emerged as a reliable strategy for the preparation of compounds with high surface to volume ratio and abundant active sites. The present study focuses in the preparation of tungsten carbide/oxide compounds deposited in a three-dimensional vertical graphene nanowalls (VGNW) substrate via chemical vapor deposition, magnetron sputtering and thermal annealing processes. Structural and chemical characterization reveals the partial carburization and oxidation of the W film sputtered on the VGNWs, due to C and O migration from VGNWs towards W during the high temperature annealing process. Electrochemical characterization shows the enhanced performance of the nanostructured hybrid W_2C/WO_x on VGNW compound towards HER, when compared with planar W_2C/WO_x films. The W_2C/WO_x nanoparticles on VGNWs require an overpotential of −252 mV for the generation of 10 mA cm^{-2}. Chronoamperometry tests in high overpotentials reveal the compounds stability while sustaining high currents, in the order of hundreds of mA. Post-chronoamperometry test XPS characterization unveils the formation of a W hydroxide layer which favours hydrogen evolution in acidic electrolytes. We aspire that the presented insights can be valuable for those working on the preparation of hybrid electrodes for electrochemical processes.

1. Introduction

Summer of 2023 has been recorded as the hottest ever, especially in the north hemisphere. An outcome of the above has been the

burst of ocean storms, wildfires, flooding, and droughts [1]. To tackle climate change, it is urgent to develop environmentally sustainable energy generation and storage technologies, as means to achieve enviromental and ultimately economic security. The exhaustible nature of fossil fuels places our society in seek for alternative and renewable energy carriers [2]. In the above context, hydrogen has attracted significant attention, as it is the most abundant resource in the universe, while it holds the highest specific energy density of any known fuel (~120–142 MJ/kg). In addition, hydrogen is a clean fuel that, when consumed in a fuel cell, produces only water, electricity and heat. Nowadays, H_2 is mainly produced by i) natural gas steam reforming and ii) methanol reforming. Nevertheless, the first route does not consist of a renewable energy source, while methane reforming results in the production of CO_2, which contributes to the greenhouse effect. Thus, the above routes are not sufficient to meet the energy demands of a post-fossil fuel driven society while preventing global warming. Moreover, projections of demand for the next decades estimate a 5-fold increase in hydrogen demand until 2050. If EU aims in meeting the targets of the Paris agreement to keep global warming below 1.8 °C, a higher demand is foreseen, up to a 10-fold increase according to European Hydrogen Roadmap [3]. Similar trends are foreseen by PwC in global scale [4]. Water splitting through electrolysis is an environmentally responsible, carbon-free alternative technique for hydrogen generation. Hydrogen resulting from this process is denominated as green hydrogen, to distinguish it from hydrogen produced through the above-mentioned methods. Water splitting takes place in an electrolytic cell and requires a potential difference of 1.23 V to occur. The hydrogen evolution reaction (HER) and oxygen evolution reaction (OER) occur at the cathode and the anode of the cell, producing gaseous hydrogen and oxygen molecules, respectively. Theoretically, the HER requires no overpotentials and can occur at 0 V. Nevertheless, in practice, increased negative potential values are required to initiate the reaction, due to sluggish reaction kinetics or other non-ideal conditions [5]. Heterogeneous electrocatalysis is a process that can accelerate these electrochemical reactions on the surface of catalysts materials, promoting their initialization in lower potentials and under higher rates. For the production of H_2, the design and development of efficient catalysts towards HER is of fundamental importance [6]. Up today, noble metals of the platinum group (like Rh, Pt, Ru) are the most attractive electrocatalysts for HER, as they possess low overpotentials, low Tafel slopes, high exchange current densities, and remarkable stabilities in water reduction reactions. Nevertheless, the high cost and scarcity of these materials limit their potential applications [7].

Therefore, strong efforts are put in the development of alternative materials that can replace the noble metals family as electrolysers. These materials should be of low cost and do not compromise the electrocatalytic efficiency. Lately, a lot of attention has been paid to transition metals carbides (TMCs), like Mo_2C, TaC and WC [8–10]. TMCs have a favourable electronic structure, as the metal-carbon bond formation modifies the transition metal d-band structure, resembling the band structure of Pt [11]. To further improve electrode's activity, TMCs are combined with carbon and graphene supports that offer high surface area, good electrical conductivity and facilitate enhanced catalyst loading. The resulting hybrid composites show superior performance accompanied by durability [12,13]. W_2C and W oxide-based compounds have emerged as potential candidates for Pt replacement [14,15]. WC compounds in the form of nanoparticles have been deposited on conductive graphene nanoplatelets [16] and carbon nanotubes (CNTs) [17]. Nevertheless, poor contact resistance between WC and conductive substrates can alter the electrocatalytic efficiency of the compound [18,19].

To overcome the above challenges, here, we proceed with the preparation of hybrid compounds of W_2C/WO_x (where x: 2 or 3) deposited on VGNWs. VGNWs show high specific surface area, comparable to this of CNTs, excellent electrical conductivity, scalability, and compatibility with transition metal compounds, which make them an ideal support system for the deposition of WC [20]. VGNWs are deposited through chemical vapor deposition, using CH_4 as a precursor gas, and elemental W is deposited on them via magnetron sputtering in Ar atmosphere. Both precursors and used technologies are affordable and easily scalable to meet industrial demands, which makes the present electrocatalyst very appealing for use in a wide scale. W_2C/WO_x is formed during a high temperature annealing step. The VGNWs provide C and O species that migrate towards W and react with it. The resulting compounds can be directly applied as electrocatalysts in the HER. Electrochemical analysis results make evident some important findings, related to the electrocatalytic performance of W_2C/WO_x on VGNWs towards HER. These are (i) the benefit of using VGNWs as a support template, compared to a planar graphitic substrate and (ii) the enhancement of performance after the formation of W nanoparticles, compared to the performance of bulk W coatings.

2. Experimental part

Synthesis of Vertical Graphene Nanowalls (VGNWs) on Papyex paper: The deposition of VGNWs on commercial Papyex paper was achieved through inductively coupled plasma-chemical vapor deposition (ICP-CVD). A comprehensive synthesis process description can be found in existing literature [21]. Briefly, the deposition setup consisted of an ICP-CVD system (13.56 MHz, power = 440 W), which included a quartz tube, a radio frequency (RF) resonator for generating remote plasma, and a tubular oven. Papyex paper was purchased by Mersen. It is composed of graphitic crystals with a nonpreferred orientation, exhibits a high specific absorption surface area, as well as very good mechanical and chemical stability. The Papyex foil was cut into rectangular pieces measuring 3*4 cm. Prior to introduction into the reactor, these pieces were meticulously cleaned using isopropanol and distilled water, followed by thorough drying. During the deposition process, the sample was positioned approximately 30 cm away from the plasma zone and heated in a temperature of 750 °C, while concurrently reducing the reactor pressure to around 10^{-4} mTorr using a turbomolecular pump. The initial step involved the cleaning of the Papyex surface through exposure to H_2 plasma. This cleaning procedure entailed applying an RF power of 400 W at a pressure of 400 mTorr of H_2 for a duration of 1 min. Subsequently, the H_2 flow was discontinued, and a CH_4 plasma was generated under identical RF power and pressure conditions to initiate the growth of graphene nanowalls (VGNWs). The GNW growth process continued for 30 min. Following the growth period, the VGNWs on the Papyex sample were allowed to gradually cool down to room temperature (approximately 20 °C) within a vacuum environment. Lastly, a short-duration O_2 plasma treatment

was applied to enhance the hydrophilicity of VGNWs surface. This treatment involved applying an RF power of 40 W at a pressure of 400 mTorr for 30 s. After the process was completed, the VGNWs on the GFs sample were removed from the reactor.

Deposition of WC/WO₃: The VGNWs-on-Papyex sample was placed inside a sputtering chamber, which was directly connected to a CVD oven. To hold the sample securely, a circular segment, 5 mm thick, was cut from a graphite bar and used as a sample holder. It's important to note that the entire system, including the magnetron sputtering and the CVD oven, was integrated into a single unit. This configuration ensured that there was no separation between the sputtering chamber and the quartz oven. One of the primary advantages of this setup is its ability to deposit metals via magnetron sputtering and subsequently perform thermal annealing under vacuum conditions, all without exposing the sample to the atmosphere. A comprehensive description of this system can be found in previously published literature studies. To prepare the sample for further processing, the reactor's pressure was reduced to approximately $\sim10^{-3}$ mTorr using a turbomolecular pump. Magnetron sputtering was employed to deposit Tungsten (W) onto the VGNWs/Papyex. High-purity W material with a purity level of 99.99 % was used as the target, and the deposition was carried out at an RF power of 100 W, with an argon (Ar) pressure of 70 mTorr for varying deposition durations. The rate of W deposition on Papyex was approximately ~4 nm/min, as determined by a prior calibration process conducted on a glass substrate. Upon completion of the W deposition step, the W-on-GNW sample was carefully transferred to the quartz tube oven. The oven was gradually heated to a temperature of 980 °C while maintaining an atmospheric pressure of 7 mTorr in a pure argon (Ar) environment. Subsequently, the W-on-GNW samples underwent annealing under the same atmospheric conditions for varying durations to facilitate the carburization of the tungsten. Following the carburization process, the CVD oven system was allowed to cool down to room temperature, and the W_2C/WO_x-on-VGNW sample was extracted for subsequent characterization. For control samples in which no carburization of W occurred on the VGNWs, the sample was removed from the magnetron sputtering chamber immediately after the W deposition phase.

Physical characterization: The WC/WO₃ on VGNWs samples were subjected to examination using scanning electron microscopy (SEM) (JEOL JSM-7001F, operated at 20 kV) and transmission electron microscopy (TEM) (JEOL 1010, operated at 200 kV). The elemental composition of the samples was determined using energy-dispersive X-ray spectroscopy (EDS). For TEM observation, the nanostructures were transferred onto a Cu grid by applying pressure with a cotton stick to remove them from the growth substrate. SEM and TEM images were processed using Image J and Digital Micrograph software. X-ray photoelectron spectroscopy (XPS) was carried out using a PHI 5500 Multi-Technique System (Physical Electronics, Chanhassen, MN, USA) with a monochromatic X-ray source (Al Ka line of 1486.6 eV energy and 350 W) positioned perpendicular to the analyzer axis and calibrated using the Ag 3d5/2 line at a full-width half-maximum (FWHM) of 0.8 eV. The analyzed area was a circle with a diameter of 0.8 mm, and the selected resolution for the survey XPS spectra had a pass energy of 187.5 eV and 0.8 eV/step, while the selected resolution for the elemental spectra had a pass energy of 11.75 eV and 0.1 eV/step. The vibrational modes of the WC/WO₃ on VGNWs samples were studied using a Raman microscope (HR800, Lab-Ram; HORIBA France SAS, Palaiseau, France) with a 532-nm solid-state laser (laser power = 5 mW; diameter
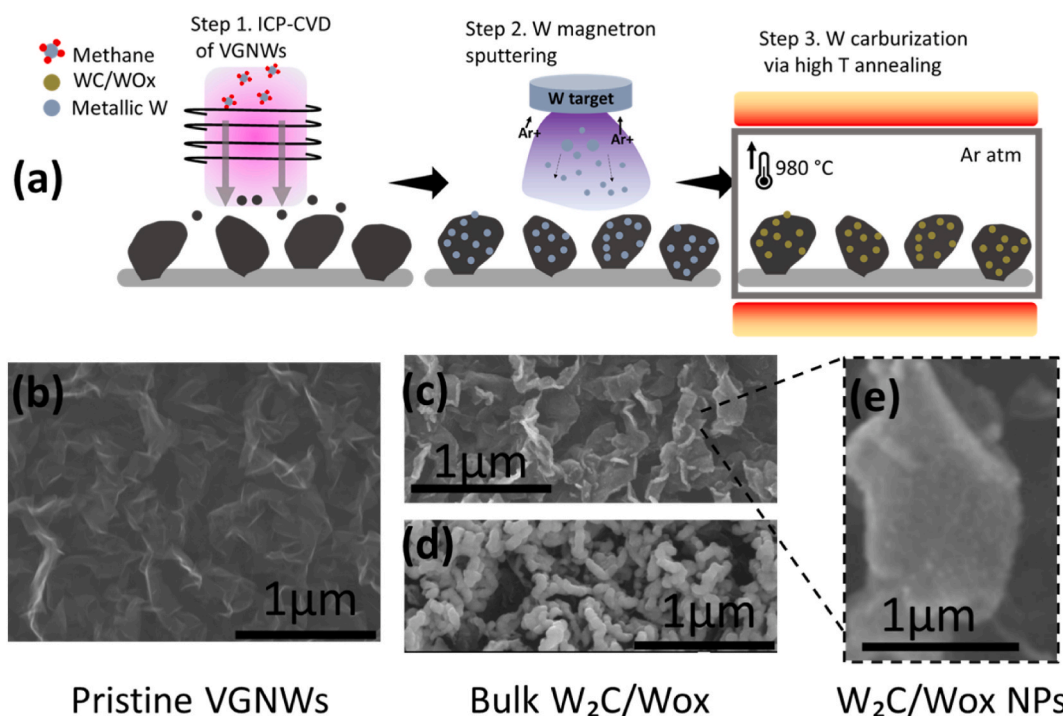
Fig. 1. a) schematic illustration of the synthesis steps that lead to the preparation of the WC/VGNWs compounds. SEM images of b) the pristine VGNWs, c) the W_2C/WO_x NPs (5 min sputtering) on VGNWs, d) the bulk W_2C/WO_x compounds (20 min sputtering) on VGNWs and e) magnified area of Fig. 1c where the WC particles deposited in the VGNWs plane are observed.

= ~1 μm). For X-ray diffraction (XRD) measurements, a PANalytical XPert PRO MPD Bragg-Brentano powder diffractometer with a 240-mm radius was used. Samples were exposed to Co Ka radiation ($\lambda = 1.789$ Å) in a 2θ range from 4 to 99° with a step size of 0.017° and a measuring time of 200 s per step.

Electrochemical characterization: The electrochemical properties of the compounds were studied using a potentiostat/galvanostat (AutoLab, PGSTAT30, Eco Chemie B.V.). All experiments were performed at room temperature in a typical three-electrode cell. An Ag/AgCl electrode (an internal 3 M KCl solution) and a Pt electrode (purchased from Metrohm; the Pt tip was separated by porous glass to avoid dissolution into the electrolyte and sample contamination) were used as the reference and counter electrodes, respectively. The working electrode was nanostructured WC deposited on the VGNWs on Papyex or WC deposited on bare Papyex support and was electrically connected to the power supply via a crocodile clip. No binder wea used, since the adhesion of both the VGNWs and WC was sufficient. Linear sweep voltammetry (LSV) was performed with a scan rate of 5 mV s^{-1} in a 0.5 M H$_2$SO$_4$ electrolyte. The surface area of the electrodes was always 1 cm^2. LSV measurements were performed 10 times before recording the data to ensure stable performance of the electrode. All potentials were converted against the RHE using the Nernst law equation as follows: , where E$_{RHE}$ is the potential of the Reversed Hydrogen Electrode and E$_{Ag/AgCl}$ is the measured potential against the Ag/AgCl (3 M KCl) reference electrode. Charge transfer resistance was measured via electrochemical impedance spectroscopy (EIS) in the frequency range from 100 kHz to 0.1 Hz. All electrodes were stored under ambient conditions and were characterized several days to weeks after electrode preparation. All electrochemical measurements were performed at room temperature.

3. Results & discussion

Fig. 1a represents a schematic illustration with the preparation process of the composite material. A SEM image of the VGNWs deposited on the Papyex substrate is showed in Fig. 1b. The height of the VGNWs is ~ 1 μm, as measured in profile images in previous work [13]. The flake's length is in the order of hundreds of nanometers. SEM images of the W compounds deposited on the VGNWs are shown on Fig. 1c and d. Depending on the sputtering deposition duration, the morphology of the compounds varies. For a short deposition time of 5 min, W forms nanoparticles anchored on the basal planes and edges of the VGNW (Fig. 1c). For a long deposition time of 20 min, W forms a continuous film, which is deposited as a coating on the VGNWs flake (Fig. 1d). Post-deposition in-situ annealing occurs in an Ar atmosphere and in high temperature of 950 °C, during which carburization of the W compounds occurs. In accordance to what has been reported recently for Mo deposited on VGNWs, carburization of the transition metal occurs due to migration and reaction with C atoms that are loosely bonded on the VGNWs [12]. The carburization step last 10 min and does not alter the morphological characteristics (size or shape) of the W compounds. A high magnification SEM image of the W$_2$C/WO$_x$ nanoparticles anchored on the VGNWs is shown in Fig. 1e.

Raman spectroscopy characterization is used to monitor the deposition and carburization of W on VGNWs (Fig. 2). The Raman spectrum of the pristine VGNWs is depicted in black colour. The graphene D mode appears at 1345 cm^{-1}, the G appears at 1579 cm^{-1} and the 2D mode appears at 2691 cm^{-1}. The FWHM of the 2D peak is calculated to be 76 cm^{-1}, by applying a Gaussian fitting, which reveals that each individual VGNWs consists of ~6 atomic layers (black spectum) [21,22]. Upon W deposition and annealing, the FWHM of the 2D peak takes a value of 64 cm^{-1}, which indicates that VGNWs consist of 4 atomic layers (red spectrum). Meanwhile, the $\frac{I_{2D}}{I_G}$ ratio increase from 0.44, for pristine VGNWs, to 0.58, for the WC on VGNWs hybrid compound. The changes in the graphene Raman peaks indicate that a decrease in layer number of the VGNWs occurs during the annealing step. This decrease is a result of migration of loosely bonded C atoms from the VGNW to react with W. The annealing process results in a re-crystallization of the graphene lattice, which is manifested in a reduction in the D peak intensity. Thus, the $\frac{I_D}{I_G}$ ratio decreases from 0.91, for pristine VGNWs,
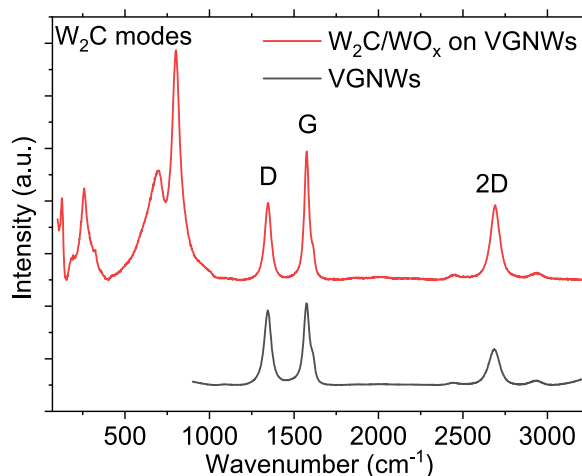
Fig. 2. Raman spectra of pristine VGNWs (black curve) and WC on VGNWs hybrid compound (red curve). They are distinguished the decrease in graphene's D peak intensity and narrowing of 2D band upon the high temperature annealing and formation of the WC compound.

to 0.60 for the WC on VGNWs hybrid compound. The decrease of the above ratio indicates the decrease on the density of structural defects on the graphene lattice, according to equation

$$n_D\left(cm^{-2}\right) = \frac{(1.8 \pm 0.5)x10^{22}x\left(\frac{I_D}{I_G}\right)}{\lambda_L^4}$$

where λ is the laser wavelength in nm [23]. A similar trend has been observed in the case of Mo_2C formation on VGNWs [12]. Moreover, various Raman modes attributed to WC and WC-O are observed between 120 and 800 cm^{-1} [24,25]. The main peaks are centred at 258, 694 and 800 cm^{-1}.

XRD characterization has been performed to detect the crystal fingerprint of the deposited compounds. In the pristine VGNWs sample, diffraction peaks associated to graphitic carbon are observed at *2θ~25.6°* (111), *2θ~52.8°* (222), *2θ~54.6°* (112), *2θ~77.5°* (−110), *2θ~83.7°* (120) and *2θ~86.9°* (333) (JCPDS file 01-075-2078) (Fig. 3, black graph). After the W deposition and carburization, diffraction peaks associated to W_2C ((100) at *2θ~34.5°*, (002) at *2θ~38°*, (110) at 61.8°, (103) at 69.7° and (101) at *2θ~39.6°* (JCPDS file 035–0776)), WO_2 ((210) at *2θ~40.5°* (JCPDS file 032–12393)) and WO_3 ((113) at *2θ~58.82°* (JCPDS file 83–0950)) are observed (Fig. 3, red graph) [26–28]. The XRD cards with the crystallographic information are presented in the supplementary materials. These results reveal the additional formation of oxide phases that were not observed in the Raman fingerprint. Apparently, oxide species that are present in the VGNWs migrate and react with W during the annealing process. Thus, the resulting hybrid compound is not a pure carbide but a hybrid structure consisting of both carbide and oxide domains.

Fig. 4 shows the results from the TEM characterization of the W_2C/WO_x nanoparticles (NPs) on the GNWs compound. They are observed nanoparticles of various crystallographic orientations deposited on the VGNWs. Fast Fourier Transformation (FFT) is applied in the TEM images to calculate the d-spacing values of the domains. In Fig. 4a, they are observed lattice fringes of WO_3, with a spacing of 0.247 nm which corresponds to the (221) orientation, lattice fringes of WO_2, with a spacing of 0.245 nm which corresponds to the (020) orientation and lattice fringes W_2C, with a spacing of 0.260 nm which corresponds to the (002) orientation [15,29]. In Fig. 4b, they are observed lattice fringes of graphene, originating from the VGNWs, with a spacing of 0.34 nm which corresponds to the (002) orientation [12]. TEM results confirm XRD results regarding the formation of hybrid W NPs, consisting of both carbide and oxide phases, anchored on the VGNWs.

The surface states of the W compounds deposited on VGNWs were characterized by XPS (Fig. 5). Fig. 5a shows the W4f peak. They are distinguished the peaks associated to the W_2C, centred at 34.3 and 32.1 eV, as well as those associated to metallic W, centred at 33.7 and 31.7 eV, respectively. Peaks associated to the oxide phase WO_3 are centred at 37.9 and 35.8 eV, respectively. The oxide phase-associated peaks are more intense compared to the carbide/metallic peaks, revealing a predominant surface oxidation taking place in the compound. The deconvolution of the W4f peaks is in agreement with the XRD results and confirms the formation of both carbide and oxide W phases upon the annealing step [30,31]. Fig. 5b shows the O1s peak. The more intense peak is this associated to the bonding between W and O, centred at 530.9 eV. Less intense peaks centred at 532.2 and 533.3 eV are associated to the bonding of O with OH and C species, respectively, originating from the CH_4 plasma process that has been used for the VGNWs synthesis [13]. Finally, Fig. 5c shows the deconvolution of the C 1s peak. The most intense peak is this corresponding to the sp^2 carbon hybrids, centred at 284.4 eV, arising from the VGNWs. Less intense peaks, shifted to higher energies, arise from sp^3 carbon hybrids as well as from hydrogenated species [32]. Detailed information regarding the XPS data, including the different elemental species, assignments due to position (binding energy), adjusted areas, FWHM of the adjustments and % area concentration of the different multiplicities, is
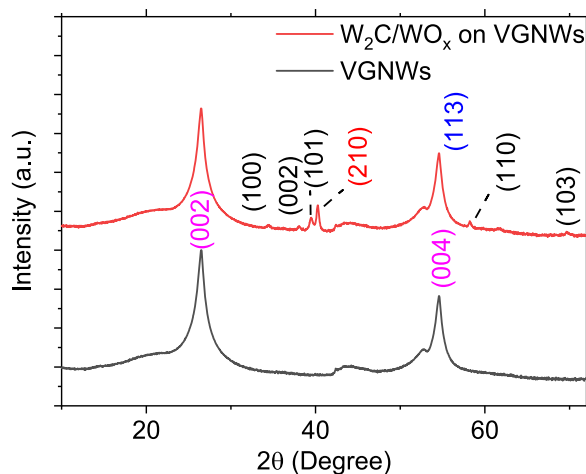
Fig. 3. XRD patterns of pristine VGNWs (black curve) and WC on VGNWs (red curves). Diffraction peaks correspond to graphite (crystal orientations depicted in magenta), W_2C (crystal orientations depicted in black), WO_3 (crystal orientations depicted in blue) and WO_2 (crystal orientations depicted in red), revealing the formation of a hybrid structure consisting of both carbide and oxide domains.
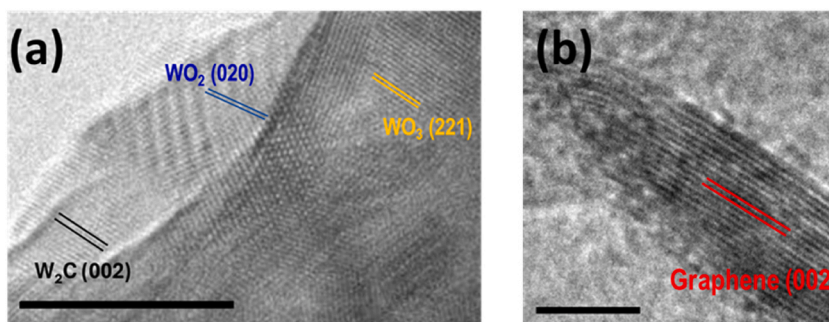
Fig. 4. HRTEM images of W_2C/WO_x NPs on VGNWs hybrid. FFT was used to calculate the spacing of lattice fringes. a) crystal structure of the WC compound. They are observed domains of WO_2, WO_3, and W_2C (scale bar is 10 nm). b) crystal structure of the VGNWs support (scale bar is 5 nm).
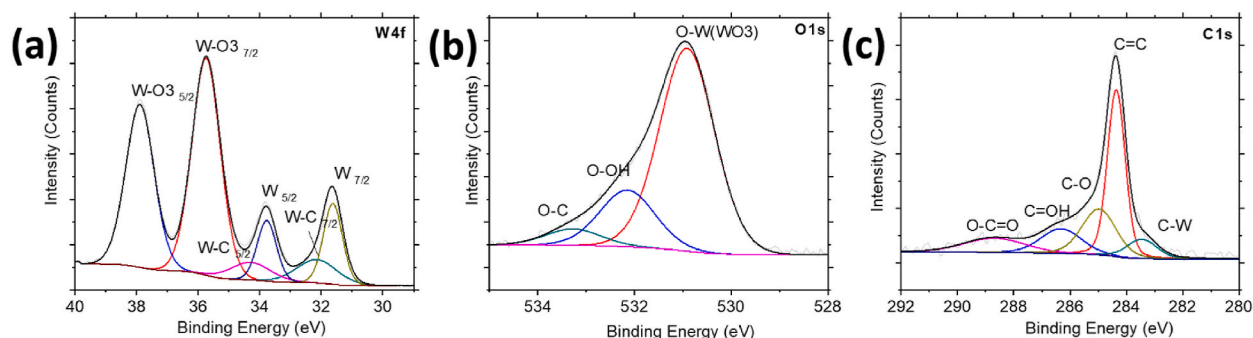
Fig. 5. XPS spectra of the pristine W_2C/WO_x NPs on VGNWs: a) W 4f spectrum, b) O 1s spectrum and c) C1s spectrum.

included in Supplementary Table 1.

The compounds are tested as working electrodes towards the HER. Results of the electrochemical characterization are shown in Fig. 6. Fig. 6a shows the linear sweep voltammetry measurements. The onset potential and overpotential required to generate 10 ma cm^{-2} are compared. The overpotential value at a current density of 10 mA cm-2 is an important reference point for the solar-light-coupled HER devices as they usually operate at such currents under standard conditions [33]. The VGNWs support (black spectrum) initiates the hydrogen evolution at an onset potential of -292 mV and requires an overpotential of -430 mV to generate a current density of 10 mA cm^{-2}. The bulk W_2C/WO_x on VGNWs hybrid electrode initiates the hydrogen evolution at an onset potential of -191 mV and requires an overpotential of -300 mV to generate a current density of 10 mA cm^{-2}. The W_2C/WO_x NPs on VGNWs hybrid electrode initiates the hydrogen evolution at an onset potential of -151 mV and requires an overpotential of -252 mV to generate a current density of 10 mA cm^{-2}. To give emphasis on the beneficial role of using the VGNWs support for the deposition of the W compounds, they are compared to a W_2C/WO_x planar film deposited directly on the Papyex substrate, under the same synthesis conditions as the above nanostructured compounds. The planar film initiates the hydrogen evolution at an onset potential of -262 mV and requires an overpotential of -392 mV to generate a current density of 10 mA cm^{-2}. Thus, the role of the GNWs support in providing an enhanced surface area for the deposition of the W compounds, compared to this of the planar substrate, appears to be highly beneficial. The activity of a Pt foil is reported for comparison. It presents an onset potential of 0 V and requires 43 mV for the generation of 10 mA cm^{-1}, in accordance with literature studies regarding hydrogen evolution with Pt catalysts in acids. In addition to the high reaction rates, the Pt foil exhibits a remarkable operation stability over 11000 s, generating 11 ± 0.5 mA under an over-potential of -45 mV (Suppl Fig. 1). Between the nanostructured compounds deposited on the VGNWs, it becomes evident that the W compounds in the form of NPs is more efficient than the bulk W compounds. To underline the superior performance of the hybrid W_2C/WO_x NPs on VGNWs, it is compared with those of pure W_2C on Papyex and Pure WO_3 on Papyex (Fig. 6b). Pure W_2C on Papyex initiates the hydrogen evolution at an onset potential of -200 mV and requires an overpotential of -382 mV to generate a current density of 10 mA cm^{-2}. Pure WO_3 on Papyex initiates the hydrogen evolution at an onset potential of -322 mV and requires an overpotential of -493 mV to generate a current density of 10 mA cm^{-2}. The XRD spectra which confirm the formation of the respected pure phases are depicted in the inset of the Figure. Fig. 6c shows the Tafel slope values extrapolated from the LSV measurements shown in Fig. 6a. The VGNWs support and W_2C/WO_x planar film exhibit Tafel slopes values of 125 and 123 mV/dec respectively. These values indicate that the Volmer step, related to the H$^+$ adsorption, limits the reaction rates [34]. The bulk W_2C/WO_x compounds and W_2C/WO_x NPs exhibit Tafel slopes values of 95 and 87 mV/dec respectively. These values, placed between 40 and 120 mV/dec, suggest a Volmer-Heyrovsky pathway, in which a H$^+$ is adsorbed on an active site on the catalyst's surface and a second H$^+$ is bonded directly with the first one, for the HER [35]. The reduced slope value exhibited by the NPs is attributed to the enhanced availability of active sites, which results in faster reaction kinetics and is in agreement the LSV results. The Pt foil exhibits a Tafel slope value of 35
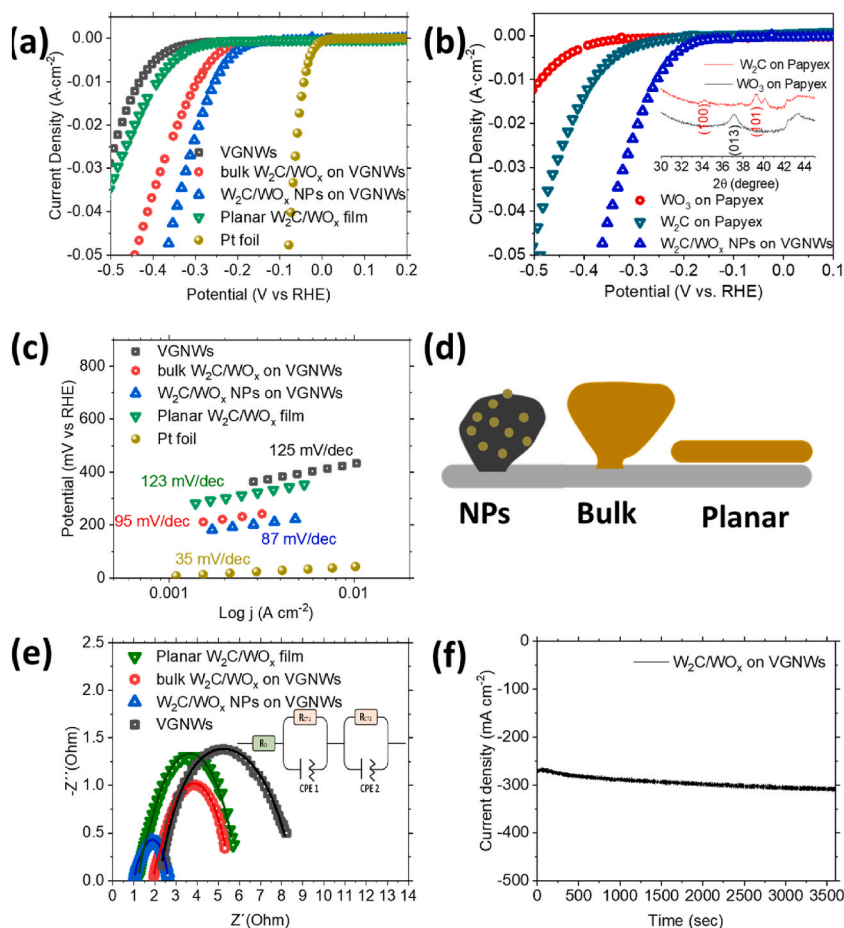
Fig. 6. a) LSV curves of pristine VGNWs (black curve), planar W_2C/WO_x film (green curve), bulk W_2C/WO_x on VGNWs (red graph) and W_2C/WO_x NPs on VGNWs (blue graph). b) LSV curves of W_2C/WO_x NPs on VGNWs (blue graph), pure W_2C on Papyex (green graph) and pure MoO_3 on Papyex (black graph) and XRD spectra of pure W_2C on Papyex (red graph) and pure MoO_3 on Papyex (black graph). c) Tafel slopes of pristine VGNWs (black curve), planar W_2C/WO_x film (green curve), bulk W_2C/WO_x on VGNWs (red graph) and W_2C/WO_x NPs on VGNWs (blue graph). d) illustrations of the nanostructures described above to serve as a guide. e) Nyquist plots of pristine VGNWs (black curve), planar W_2C/WO_x film (green curve), bulk W_2C/WO_x on VGNWs (red graph) and W_2C/WO_x NPs on VGNWs (blue graph). The fitting curves are plotted as continuous lines. f) chronoamperometry measurement of the W_2C/WO_x NPs on VGNWs compound.

mV/dec. An illustration of the compared nanostructured electrodes is presented in Fig. 6d. The above performance of the present nanostructured W compounds on VGNWs hybrids is favourably compared to this reported in previous works regarding W carbides on porous and metallic three-dimensional supports, including WC nanoparticles on glassy carbon [36], WC nanoparticles on graphite [37] and WC nanostructures deposited in Ni foam [38]. EIS characterization has been performed under a constant -400 mV bias vs RHE, to study the interfacial charge transfer kinetics. The Nyquist plots are presented in Fig. 6e. The size of the semicircle directly mirrors the magnitude of the charge transfer resistance (R_{ct}), providing a visual indicator of the impedance associated with the electron transfer kinetics at the interface of the electrocatalyst and the electrolyte [39]. The VGNWs support electrode exhibits a R_{ct} of 6.15 Ohm (black graph), the W_2C/WO_x planar film exhibits a R_{ct} of 4.57 Ohm (green graph), the bulk W_2C/WO_x compound exhibits a R_{ct} of 3.43 Ohm (red graph) and the W_2C/WO_x NPs exhibits a R_{ct} of 1.57 Ohm (blue graph). It becomes evident that the W_2C/WO_x NPs exhibit the lower R_{ct} between all samples, which justifies the superior electrolytic performance of this compound. The equivalent circuit model used to extract the resistances parameters is depicted in the inset of Fig. 6e. All parameters are presented in Table 2. A chronoamperometry test was performed in the W_2C/WO_x NPs under -0.8 V for 1 h, to evaluate the stability of the compound in very high overpotentials (Fig. 6f), since durable catalysts that could afford the industrial scale current density (>300 mA cm^{-2}) are desired for the forthcoming hydrogen economy [40]. Initially, it is generated a current of 270 mA cm^{-2}. After 1 h of continuous operation, the generated current is 310 mA cm^{-2}, which corresponds to a 14 % increase in the produced current. Upon the chronoamperometry test, the electrode has been characterised structurally and chemically, to evaluate its endurance. XRD characterization shows the presence of peaks related both to W carbide (peak centred at 39°) and W oxide (peak centred at 41°) (Fig. 7a). Nevertheless, the FWHM increases for all peaks, which reveals a decrease in the crystallite size [41]. The FWHM values of various diffraction peaks, before and after the chronoamperometry test, are listed in Table 1. SEM characterization upon the chronoamperometry test shows no degradation on the

structure of the W_2C/WO_x NPs on VGNWs compounds (Fig. 7b). Surface chemical characterization is performed by XPS. The wide scan spectrum shows no contamination of the working electrode upon the chronoamperometry test (Fig. 7c), besides a trace of S which originates from the used H_2SO_4 electrolyte. Nevertheless, changes are observed in the chemical states of the elements which compose the compounds. The W4f peaks reveal complete oxidation of the compound surface after the chronoamperometry test. The peaks related to metallic and carburized W are no more visible and only the $W_{5/2}$ and $W_{7/2}$ related to WO_3 are observed (Fig, 7 d). Based on information obtained by both XRD and XPS analysis, we believe that complete oxidation occurs only on the surface of the compound, while the underlying carbide phases remain electrocatalytically active, which justifies the endurance during the chronoamperometry test. The O 1s peaks (Fig. 7e) can be decomposed into three components: 530.5 eV from oxidic species (O^{2-}), 532.0 eV from hydroxide species (OH^-), and 533.5 eV from reaction of O with C. The evolution of the peak related to the hydroxide species shows the formation of hydroxide surface sites which favour the hydrogen evolution reaction steps and justifies the slight increase in current density during the chronoamperometry test [42]. A HRTEM image of the sample taken after the chronoamperometry test shows the lattice fringes of W_2C/WO_2 nanoparticle extending continuously from the bulk until the surface. This observation excludes the formation of an interface with a discrete hydroxide layer and points towards the formation of distinguished hydroxide surface sites, in accordance with XPS evidences (Fig. 7e). Fast Fourier Transformation of the above-mentioned Figure is used to identify the d-spacing lengths of the carbide and oxide phases. The lattice planes are marked on the Figure. The calculated d-spacing for the marked regions of the particle are 0.282 nm (red-marked planes, corresponding to 101 WO_2), 0.243 nm (white-marked planes, corresponding to 200 WO_2) and 0.277 (black-marked planes, corresponding to 101 W_2C). A post-chronoamperometry LSV measurement shows a dramatic decrease on the recorded onset and overpotential value and is associated with the formation of the hydroxide surface sites [43]. The oxidised W electrode with the hydroxide surface sites requires only -86 mV to generate 10 mA cm^{-2}. The LSV curves corresponding to the pristine and post-chronoamperometry electrodes are exhibited in Fig. 7f. Further assessment of the compound stability has been performed by chronoamperometry tests in lower overpotential values. The compound has been tested during 10 h in an applied overpotential of -190 mV, generating 1.9 mA cm^{-2}, and showed remarkable stability (Suppl Figure 2). Cyclic voltammetry tests on the compound in pristine state and after the realization of the 10 h chronoamperometry revealed a stable double-layer capacitance (Supple. Fig. 3). Moreover, the stability of the compounds has been confirmed by comparison of the LSV curves in pristine state and after realization of 1000 CV cycles in a voltage window 0–0.8 V (Supple. Fig. 4). These results confirm the great prospect of W-based compounds hybridization with graphene materials for application in electrocatalytic hydrogen evolution [44–48].

4. Conclusions

WC compounds were deposited on VGNWs supports, grown on a flexible Papyex substrate. The hybrid compounds were tested as cathode electrodes towards hydrogen evolution. W is deposited via magnetron sputtering and hybrid carbide and oxide phases are formed via C and O migration from the VGNWs during an in-situ high temperature annealing step. Regarding the W deposition, two
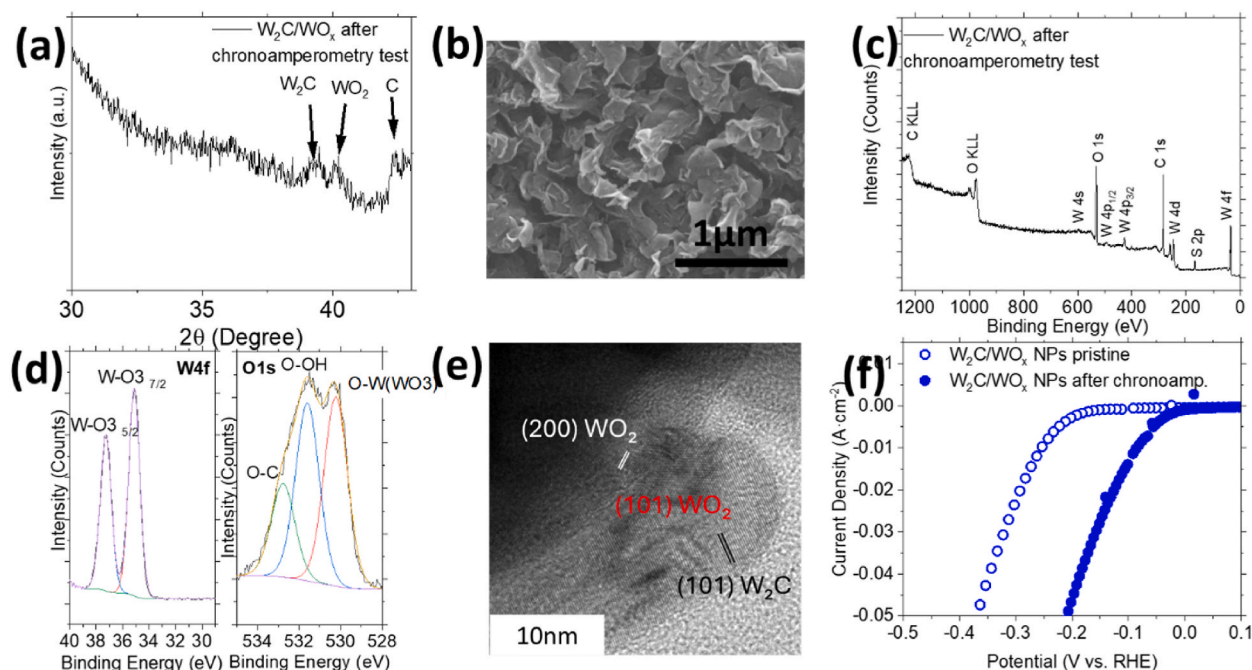
Fig. 7. Electrode characterization post chronoamperometry test: a) XRD spectrum, b) SEM image, c) wide scan of the XPS spectrum, d) W 4f peak of the XPS spectrum (left graph) and O 1s peak of the XPS spectrum (right graph), e) HRTEM images of W_2C/WO_x NPs on VGNWs hybrid after the chronoamperometry test and f) LSV curves comparison of the electrode in pristine and post-chronoamperometry test state.

Table 1

FWHM values of various diffraction peaks of the W_2C/WO_x compound in pristine and after chronoamperometry test states.

Peak	Position (°)	FWHM (°) pristine	FWHM (°) after chronoamperometry
W_2C (101)	39.6	0.57	0.72
WO_2 (210)	40.5	0.36	0.68
W_2C (110)	61.8	1.03	2.52

Table 2

Equivalent circuit parameters obtained from fitting the EIS data. CPE_T is the amplitude of the constant phase element. CPE_P values are related to the resistance or capacitive nature of the CPE (values closer to 0 correspond to an ideal resistor, values closer to 1 correspond to an ideal capacitor).

Electrode Material	R_Ω (Ohm)	R_{CT1} (Ohm)	CPE_T-CPE_P 1		R_{CT2} (Ohm)	CPE_T-CPE_P 2	
VGNWs	2.19	1.86	0.003	0.68	4.59	0.012	0.54
Planar W_2C/WOx film	1.23	0.17	0.001	0.99	4.53	0.008	0.67
bulk W_2C/WOx on VGNWs	1.95	0.16	0.001	0.96	3.46	0.012	0.67
W_2C/WOx NPs on VGNWs	1.04	0.11	0.00	1.00	1.49	0.013	0.66

Toc

regimes can stand out. In short deposition times (~5 min) W forms NPs deposited homogeneously on the VGNWs support. On long deposition times ($\geq$10 min) W forms a continuous coating over the VGNWs (denominated as bulk W compounds). Electrochemical characterization shows that the W_2C/WO_x NPs are the most efficient structures to catalyse HER, since they provide an abundance of active sites, require the lowest overpotential values and exhibit the lowest Tafel slope and R_{ct} values, compared to the bulk W_2C/WO_x compounds and W_2C/WO_x planar films. They require an overpotential of -252 mV for the generation of 10 mA cm^{-2} and a Tafel slope value of 87 mV/dec. Moreover, the W_2C/WO_x NPs show remarkable stability and an increase in catalytic efficiency during the chronoamperometry test under high constant bias capable to generate hundreds of mA. Surface chemical characterization upon the chronoamperometry reveals the formation of W hydroxide surface sites that acts as a highly active HER electrocatalyst in strong acid conditions. The synergy between W compounds and VGNWs results in a significant improvement in catalytic performance, positioning this combination as a promising candidate for upcoming clean energy technologies. These findings are anticipated to offer valuable insights into the synthesis of TMCs/graphene hybrids and enhance our understanding of graphene's role in facilitating electrocatalytic reactions.

Data availability statement

Data will be made available on request.

CRediT authorship contribution statement

Shahadev Rodriguez-Miguel: Methodology, Investigation. **Yang Ma:** Investigation. **Ghulam Farid:** Investigation. **Roger Amade:** Supervision, Resources, Methodology, Formal analysis. **Rogelio Ospina:** Methodology, Investigation. **Jose Luis Andujar:** Supervision, Methodology, Conceptualization. **Enric Bertran-Serra:** Writing – review & editing, Writing – original draft, Resources, Methodology, Funding acquisition, Formal analysis, Conceptualization. **Stefanos Chaitoglou:** Writing – review & editing, Writing – original draft, Methodology, Investigation, Formal analysis, Data curation, Conceptualization.

Declaration of competing interest

The authors declare that they have no known competing financial interests or personal relationships that could have appeared to influence the work reported in this paper.

Appendix A. Supplementary data

Supplementary data to this article can be found online at https://doi.org/10.1016/j.heliyon.2024.e31230.

References

[1] Nasa, in: NASA Announces Summer 2023 Hottest on Record, 2023. https://climate.nasa.gov/news/3282/nasa-announces-summer-2023-hottest-on-record/.
[2] N.S. Lewis, D.G. Nocera, Powering the planet: chemical challenges in solar energy utilization, Proc. Natl. Acad. Sci. USA 103 (2006) 15729–15735.
[3] https://www.clean-hydrogen.europa.eu/.
[4] https://www.pwc.com/gx/en/industries/energy-utilities-resources/future-energy/green-hydrogen-cost.html.
[5] F. Yu, L. Yu, I.K. Mishra, Y. Yu, Z.F. Ren, H.Q. Zhou, Recent developments in earth-abundant and non-noble electrocatalysts for water electrolysis, Mater. Today Phys. 7 (2018) 121–138.
[6] D. Heard, A. Lennox electrode materials in modern organic electrochemistry, Angew. Chem. Int. Ed. 59 (2020) 18866–18884.
[7] Z. Chen, X. Duan, W. Wei, S. Wang, B.-J. Ni, Recent advances in transition metal-based electrocatalysts for alkaline hydrogen evolution, J. Mater. Chem. A 7 (2019) 14971–15005.
[8] S. Chaitoglou, T. Giannakopoulou, D. Tsoutsou, C.T. Antonios Vavouliotis, A. Dimoulas, Direct versus reverse vertical two-dimensional Mo_2C/graphene heterostructures for enhanced hydrogen evolution reaction electrocatalysis, Nanotechnology 30 (2019) 415404.
[9] S. Chaitoglou, T. Giannakopoulou, T. Speliotis, A. Vavouliotis, C. Trapalis, A. Dimoulas, Mo_2C/graphene Heterostructures: Low Temperature Chemical Vapor Deposition on Liiud Bimetallic and Hydrogen Evolution Reaction Electrocatalytic Properties Nanotechnology, vol. 30, 2019 125401.
[10] S. Chaitoglou, T. Giannakopoulou, G. Papanastasiou, D. Tsoutsou, A. Vavouliotis, C. Trapalis, A. Dimoulas, Cu vapor-assisted formation of nanostructured Mo_2C electrocatalysts via direct chemical conversion of Mo surface for efficient hydrogen evolution reaction applications, Appl. Surf. Sci. 510 (2020) 145516.
[11] J.R. Kitchin, J.K. Nørskov, M.A. Barteau, J.G. Chen, Trends in the chemical properties of early transition metal carbide surfaces: a density functional study, Catal. Today 105 (2005) 66–73.
[12] S. Chaitoglou, R. Amade, E. Ospína, E. Bertran-Serra, Hybrid nanostructured compounds of Mo_2C on vertical graphene nanoflakes for a highly efficient hydrogen evolution reaction, ACS Appl. Energy Mater. 6 (2023) 6120–6131.
[13] S. Chaitoglou, R. Amade, E. Bertran-Serra, Insights into the inherent properties of vertical graphene flakes towards hydrogen evolution reaction, Appl. Surf. Sci. 592 (2022) 153327.
[14] J. Huang, W. Hong, J. Li, B. Wang, W. Liu, High-performance tungsten carbide electrocatalysts for the hydrogen evolution reaction, Sustain. Energy Fuels 4 (2020) 1078.
[15] T. Wondimu, A. Bayeh, D. Kabtamu, Q. Xu, P. Leung, A. Shah, Recent progress on tungsten oxide-based materials for the hydrogen and oxygen evolution reactions, Int. J. Hydrogen Energy 47 (2022) 20378–20397.
[16] W.F. Chen, J.M. Schneider, K. Sasaki, C.H. Wang, J. Schneider, S. Iyer, S. Iyer, Y. Zhu, J.T. Muckerman, E. Fujita, Tungsten carbide-nitride on graphene nanoplatelets as a durable hydrogen evolution electrocatalyst, ChemSusChem 7 (2014) 2414–2418.
[17] Q. Gong, Y. Wang, Q. Hu, J. Zhou, R. Feng, P.N. Duchesne, P. Zhang, F. Chen, N. Han, Y. Li, C. Jin, Y. Li, S. Lee, Ultrasmall and phase-pure W_2C nanoparticles for efficient electrocatalytic and photoelectrochemical hydrogen evolution, Nat. Commun. 18 (2016) 13216.
[18] D. Ham, R. Ganesan, J. Lee, Tungsten carbide microsphere as an electrode for cathodic hydrogen evolution from water, Int. J. Hydrogen Energy 33 (2008) 6865–6872.
[19] L. Han, M. Xu, Y. Han, Y. Yu, S. Dong, Core–shell-structured tungsten carbide encapsulated within nitrogen-doped carbon spheres for enhanced hydrogen evolution, ChemSusChem vol. 9 (2016) 2784–2787.
[20] E. Bertran-Serra, S. Rodriguez-Miguel, Z. Li, Y. Ma, G. Farid, S. Chaitoglou, R. Amade, R. Ospina, J.L. Andújar, Advancements in plasma-enhanced chemical vapor deposition for producing vertical graphene nanowalls, Nanomaterials 13 (2023) 2533.
[21] E. Bertran-Serra, A. Musheghyan-Avetisyan, S. Chaitoglou, R. Amade-Rovira, I. Alshaikh, F. Pantoja-Suarez, J.L. Andújar-Bella, T. Jawhari, A. Perez-del-Pino, E. Gyorgy, Temperature-modulated synthesis of vertically oriented atomic bilayer graphene nanowalls grown on stainless steel by inductively coupled plasma chemical vapor deposition, Appl. Surf. Sci. 610 (2022) 155530.
[22] Y. Hao, Y. Wang, L. Wang, Z. Ni, Z. Wang, R. Wang, C.K. Koo, Z. Shen, J.T.L. Thong, Probing Layer Number and Stacking Order of Few-Layer Graphene by Raman Spectroscopy Small, vol. 6, 2010, pp. 195–200.
[23] L. Cancado, A. Jorio, E.M. Ferreira, F. Stavale, C. Achete, R. Capaz, M. Moutinho, A. Lombardo, T. Kulmala, A. Ferrari, Quantifying defects in graphene via raman spectroscopy at different excitation energies, Nano Lett. vol. 11 (2011) 3190–3196.
[24] B.B. Nayak, T. Dash, S. Pradhan, Spectroscopic evaluation of tungsten carbide-titanium carbide composite prepared by arc plasma melting, J. Electron. Spectrosc. Relat. Phenom. 245 (2020) 146993.
[25] S. El Mrabet, M.D. Abad, C. López-Cartes, D. Martínez-Martínez, Sánchez-lópez thermal evolution of WC/C nanostructured coatings by Raman and in situ XRD analysis, Plasma Process. Polym. 6 (2009) S444–S449.
[26] R. Hatel, M. Baitoul, Nanostructured tungsten trioxide (WO3): synthesis, structural and morphological investigations, in: IOP conf. Series: Journal of Physics: conf. Series, 1292, 2019 012014.
[27] B. Gabhale, A. Jadhawar, A. Bhorde, S. Nair, H. Borate, R. Waykar, R. Aher, P. Sharma, A. Pawbake, S. Jadkar, High band gap nanocrystalline tungsten carbide (nc-WC) thin films grown by hot wire chemical vapor deposition (HW-CVD) method J. Nano- electron. Phys 10 (2018) 03001.
[28] R. Balzer, V. Drago, W.H. Schreiner, L. F. D. Probst, Synthesis and structure-activity relationship of a WO_3 catalyst for the total oxidation of BTX, J. Braz. Chem. Soc. 25 (2014) 2026–2031.
[29] S. Hussain, I. Rabani, D. Vikraman, A. Feroze, M. Ali, Y.S. Seo, H.Se Kim, S.H. Chun, J. Jung, One-pot synthesis of W_2C/WS_2 hybrid nanostructures for improved hydrogen evolution reactions and supercapacitors, Nanomaterials 10 (2020) 1597.
[30] J. Song, S. Kwon, Reaction mechanism and strategy for optimizing the hydrogen evolution reaction on single-layer 1T' WSe(2) and WTe(2) based on grand canonical potential kinetics, ACS Appl. Mater. Interfaces 13 (2021) 55611e20.
[31] P.V. Krasovskii, O.S. Malinovskaya, A.V. Samokhin, Y.V. Blagoveshchenskiy, V.A. Kazakov, A.A. Ashmarin, XPS study of surface chemistry of tungsten carbides nanopowders produced through DC thermal plasma/hydrogen annealing process, Appl. Surf. Sci. 339 (2015) 46–54.
[32] J. Diaz, G. Paolicelli, S. Ferrer, F. Comin, Separation of the sp^3 and sp^2 components in the C 1s photoemission spectra of amorphous carbon films, Phys. Rev. B 54 (1996) 8064.
[33] B. Joo, H. Sang, Recent advances in unveiling active sites in molybdenum sulfide based electrocatalysts for the hydrogen evolution reaction, Nano Convergence 4 (2017) 19.
[34] J. Wei, M. Zhou, A. Long, Y. Xue, H. Liao, C. Wei, Z. Xu, Heterostructured electrocatalysts for hydrogen evolution reaction under alkaline conditions, Nano-Micro Lett. 10 (2018) 75.
[35] Z. Liu, Y. Li, J. Fang, Qi wan investigation of nanoscale tungsten carbide enhanced surface carbon as a platinum support for the hydrogen, Evol. Reaction Nanomater. 13 (2023) 1369.
[36] S. Emin, C. Altinkaya, A. Semerci, H. Okuyucu, A. Yildiz, P. Stefanov, Tungsten carbide electrocatalysts prepared from metallic tungsten nanoparticles for efficient hydrogen evolution, Appl. Catal. B Environ. 236 (2018) 147–153.

[37] C. Tyagi, C. Lagrost, V. Dorcet, F. Tessier, B. Fabre, Carbon-embedded tungsten carbide electrocatalysts derived from self deposited tungsten oxide for the pH-universal hydrogen evolution reaction, ACS Appl. Energy Mater. 6 (2023) 6842–6850.

[38] F. Wang, Y. Wu, B. Dong, K. Lv, Y. Shi, N. Ke, L. Hao, L. Yin, Y. Bai, X. Xu, Y. Xian, Simeon agathopoulos robust porous WC-based self-supported ceramic electrodes for high current density hydrogen evolution reaction, Adv. Sci. 9 (2022) 2106029.

[39] S. Chaitoglou, R. Ospina, Y. Ma, R. Amade, X. Vendrell, J. Rodriguez-Pereira, E. Bertran-Serra, Deposition and in-situ formation of nanostructured Mo_2C nanoparticles on graphene nanowalls support for efficient electrocatalytic hydrogen evolution, J. Alloys Compd. 972 (2024) 172891.

[40] Y. Zhang, K.E. Arpino, Q. Yang, N. Kikugawa, D.A. Sokolov, C.W. Hicks, J. Liu, C. Felser, G. Li, Observation of a robust and active catalyst for hydrogen evolution under high current densities, Nat. Commun. 13 (2022) 7784.

[41] J.I. Langford, A.J.C. Wilson, Scherrer after sixty years: a survey and some new results in the determination of crystallite size, J. Appl. Crystallogr. 11 (1978) 102–113.

[42] A.K. Nayak, M. Verma, Y. Sohn, P.A. Deshpande, D. Pradhan, Active tungsten oxide nanoplate electrocatalysts for the hydrogen evolution reaction in acidic and near neutral electrolytes, ACS Omega 2 (2017) 7039–7047.

[43] X. Yang, F. Zhao, Y. Yeh, R.S. Selinsky, Z. Chen, N. Yao, C.G. Tully, Y. Ju, B.E. Koel, Nitrogen-plasma treated hafnium oxyhydroxide as an efficient acid-stable electrocatalyst for hydrogen evolution and oxidation reactions, Nat. Commun. 10 (2019) 1543.

[44] Y. Dang, L. Feng, W. Hu, W. Wang, Q. Zhang, B. Ma, A 3D flower-like WC with large capacitance as efficient co-catalyst in photocatalytic H_2 evolution, Int. J. Hydrogen Energy 46 (2021) 39251–39261.

[45] X. Deng, H. Chang, G. Zhang, N-doped graphene supported W_2C/WC as efficient electrocatalyst for hydrogen evolution reaction, Int. J. Hydrogen Energy 47 (2022) 902–916.

[46] A. Laszczyńska, W. Tylus, I. Szczygieł, Electrocatalytic properties for the hydrogen evolution of the electrodeposited Ni–Mo/WC composites, Int. J. Hydrogen Energy 46 (2021) 22813–22831.

[47] F. Zhang, L. He, H. Pan, S. Lian, M. Wang, J. Yin, X. Chen, J. Ren, M. Chen, Revealing the catalytic micro-mechanism of Mon, WN and WC on hydrogen evolution reaction, Int. J. Hydrogen Energy 46 (2021) 23615–23628.

[48] C.B. Rodella, D.H. Barrett, S.F. Moya, S.J.A. Figueroa, M.T.B. Pimenta, A.S. Curvelo, V. Teixeira da Silva, Physical and Chemical Studies of Tungsten Carbide Catalysts: Effects of Ni Promotion and Sulphonated Carbon, RSC Adv. vol. 5 (2015) 23874.